Monthly Notices
of the
ROYAL ASTRONOMICAL SOCIETY

MNRAS **518,** 2088–2101 (2023)
Advance Access publication 2022 November 11

https://doi.org/10.1093/mnras/stac3211

Testing the evolutionary pathways of galaxies and their supermassive black holes and the impact of feedback from active galactic nuclei via large multiwavelength data sets

George Mountrichas[1]★ and Francesco Shankar[2]★

[1]*Instituto de Fisica de Cantabria (CSIC-Universidad de Cantabria), Avenida de los Castros, Santander 39005, Spain*
[2]*School of Physics and Astronomy, University of Southampton, Highfield SO17 1BJ, UK*

Accepted 2022 November 3. Received 2022 November 3; in original form 2022 September 27

ABSTRACT

It is still a matter of intense debate how supermassive black holes (SMBHs) grow and the role played by feedback from active galactic nuclei (AGN) in the coevolution of SMBHs and galaxies. To test the coevolution proposed by theoretical models, we compile a large AGN sample of 5639 X-ray detected AGN, over a wide redshift range, spanning nearly three orders of magnitude in X-ray luminosity. The AGN have been detected in the *COSMOS-Legacy*, the Boötes, the XMM-*XXL,* and the eROSITA Final Equatorial Depth Survey (eFEDS) fields. Using the specific star formation rate estimates, we split the AGN host galaxies into star forming (SF), starburst (SB), and quiescent (Q). Our results show that the AGN accretion is increased in SB systems compared to SF and Q. Our analysis reveals a mild increase of L_X with M_*. The L_X/star formation rate (SFR) ratio has a weak dependence on M_* and at fixed M_* it is highest in Q systems. The latter trend is mostly driven by the significant drop in SFR in the Q state. The measured strong variations in SFR from the SB/SF to Q mirror those predicted in merger models with AGN feedback. However, the observed mild variations in L_X are at variance with the same models. We also study the evolution of SFR for a galaxy control sample and found that it is very similar to that of X-ray AGN. This suggests that either AGN play a minor role in the star formation quenching, or the relative timescales of the two processes are different.

Key words: galaxies: active – galaxies, galaxies: evolution – galaxies, galaxies: star formation – galaxies, X-rays: galaxies – resolved and unresolved sources as a function of wavelength.

1 INTRODUCTION

Correlations have been observed in the local (e.g. Magorrian et al. 1998; Ferrarese & Merritt 2000) and sometimes in the distant Universe (e.g. Suh et al. 2020), between the mass of the central supermassive black hole (SMBH) and several properties of the host galaxies, or even of the host dark matter haloes (e.g. Shankar et al. 2020). These correlations are often not well established, possibly affected by biases (e.g. Bernardi et al. 2007; Shankar et al. 2016; Shankar, Bernardi & Sheth 2017; Shankar et al. 2019), varying with galaxy morphology (e.g. Suh et al. 2019) and/or with the degree of activity of the central SMBH (e.g. Reines & Volonteri 2015) and often presenting significant dispersions (e.g. Graham 2016). Although some degree of correlation undoubtedly exists between SMBH and host galaxy, pinning down the physical causes driving their evolution remains elusive just relying on current observational constraints of their scaling relations. Indeed, many theoretical models show strong degeneracies when comparing with present-day data (e.g. Habouzit et al. 2021, 2022).

A step further in our understanding of SMBH growth within galaxies can be performed by directly analysing samples of Active Galactic Nuclei (AGN), when the SMBHs become active at different accretion rates at different epochs, and knowledge of their host galaxies are available. Cold gas in the galaxy can indeed fuel star formation rate (SFR) as well as accrete onto the central SMBH triggering the AGN, thus correlations between SFR and SMBH accretion rate, as recorded in the AGN luminosity, are expected.

Semi-analytic models and hydrodynamical simulations have studied the star formation and the growth of the black hole in galaxy mergers. According to most of these studies, after the starburst (SB) phase that is triggered by the merger, both the star formation and the black hole accretion rate (BHAR) are quenched. The magnitude of the suppression depends on the mass of the galaxy, with more massive systems to present a steeper decrease of both the accretion rate and the star formation (e.g. Di Matteo, Springel & Hernquist 2005; Hopkins 2012). In the case of black holes the decrease of their accretion rates is due to the accretion energy that is released. The star formation is suppressed by outflows generated by strong winds, produced by the AGN (e.g. DeBuhr, Quataert & Ma 2012) that remove or heat the star forming gas. However, this AGN feedback can work both ways (e.g. Zinn et al. 2013). For instance, in the late gas-poor phase, AGN feedback may quench star formation. In the gas-rich phase, AGN outflows can overcompress cold gas and thus enhance star formation (e.g. Zubovas et al. 2013).

From the observational point of view, previous works found that the average SMBH growth rate follows similar trends with stellar mass, M_*, and redshift as the star formation rates (SFRs) of their host galaxies (e.g. Mullaney et al. 2012; Yang et al. 2018). However, a stronger correlation has been found between the BHAR and the

★ E-mail: gmountrichas@gmail.com (GM); F.Shankar@soton.ac.uk (FS)

SFR rather than M_*, at least for AGN hosted by bulge dominated (BD) systems (Yang et al. 2019). Study of the BHAR/SFR ratio revealed that it scales weakly with M_* (e.g. Rodighiero et al. 2015; Yang et al. 2018; Carraro et al. 2020), at least for star forming (SF) and starburst (SB) galaxies (but see Mullaney et al. 2012), whereas a flat relation is found for Q systems (Carraro et al. 2020). A drop of the BHAR/SFR ratio is found during the SB phase of galaxies (Rodighiero et al. 2015), at odds with the theoretical predictions. Although, the AGN activity is enhanced in compact, SF galaxies, the bulk of the black hole growth takes place in extended, Q systems (Aird, Coil & Kocevski 2022). Moreover, the mean $L_X - M_*$ relation is independent of the AGN duty cycle, but depends strongly on the shape, normalization and scatter of the underlying $M_{BH} - M_*$ scaling relation and on the characteristic Eddington ratio (Carraro et al. 2022).

In this work, we use X-ray detected AGN in four fields, namely, the the Boötes, *COSMOS-Legacy*, the XMM-*XXL* and the eFEDS fields. Our sample consists of more than 5500 X-ray sources, spanning a redshift range of $0.5 < z < 2.5$ and nearly three orders of magnitude in X-ray luminosity, whereas their stellar mass ranges from $10.0 < \log[M_*(M_\odot)] < 12.0$. The samples used in our analysis are described in Section 2. In Section 3, we present the method we apply [spectral energy distribution (SED) fitting] to measure the host galaxy properties (SFR, M_*) and the various selection criteria we use to select only AGN with robust host galaxy measurements that also satisfy the mass completeness limits of each survey. We also describe how we classify sources into SB, SF, and Q systems. Our goal is to study the X-ray luminosity (Section 4.1) and the L_X/SFR ratio (Section 4.2), as a function M_* and compare our observational results with the predictions of theoretical models (Section 5). Our conclusions are presented in Section 6.

Throughout this work, we assume a flat ΛCDM cosmology with $H_0 = 70.4\,\mathrm{Km\,s^{-1}\,Mpc^{-1}}$ and $\Omega_M = 0.272$ (Komatsu et al. 2011).

2 DATA

In our analysis, we use X-ray AGN detected in four fields, namely, the Boötes, the COSMOS-Legacy, the eFEDS, and the XMM-XXL-N fields. The data sets are described in detail in Mountrichas et al. (2021c), Mountrichas et al. (2022b), Mountrichas et al. (2022c), and Masoura et al. (2018) papers, respectively.

Very good photometric coverage is essential to obtain robust measurements of host galaxy properties (SFR, M_*), via SED fitting (see Section 3). Therefore, all sources used in our analysis meet strict photometric selection requirements. Specifically, all sources have measurements in the following photometric bands: *u*, *g*, *r*, *i*, *z*, J, H, K, W1, or IRAC1, W2, or IRAC2, and W4 or MIPS/24, where IRAC1, IRAC2, MIPS/24 are the 3.6, 4.5, and 24 μm photometric bands of *Spitzer* and W1, W2, and W4 are the WISE photometric bands at 3.4, 4.6, and 22 μm. Approximately 35 per cent of the AGN also have available far-IR photometry (*Herschel*). Mountrichas et al. (2021b), Mountrichas et al. (2021c), and Mountrichas et al. (2022b) used data from the XMM-*XXL*, Boötes and COSMOS fields and utilizing the CIGALE (Boquien et al. 2019; Yang et al. 2020, 2022) SED fitting code, showed that lack of far-infrared (IR) photometry does not affect the SFR calculations derived by CIGALE.

We also exclude from our analysis sources with bad SED fits and unreliable host galaxy measurements (see Section 3.1). Furthermore, only AGN that satisfy the mass completeness limits of each survey are included in our measurements. These limits have been calculated following the method described in Pozzetti et al. (2010). The process is described in detail in Sections 3 of Mountrichas et al. (2021c), Mountrichas et al. (2022b), Mountrichas et al. (2022c). Below we give a brief description of each data set.

2.1 COSMOS

The *COSMOS-Legacy* survey (Civano et al. 2016) is a 4.6 Ms *Chandra* program that covers 2.2 deg^2 of the COSMOS field (Scoville et al. 2007). The central area has been observed with an exposure time of ≈160 ks, while the remaining area has an exposure time of ≈80 ks. The limiting depths are 2.2×10^{-16}, 1.5×10^{-15}, and 8.9×10^{-16} erg cm^{-2} s^{-1} in the soft (0.5–2 keV), hard (2–10 keV), and full (0.5–10 keV) bands, respectively. The X-ray catalogue includes 4016 sources. Marchesi et al. (2016) matched the X-ray sources with optical and IR counterparts using the likelihood ratio technique (Sutherland & Saunders 1992). Of the sources, 97 per cent have an optical and IR counterpart and a photometric redshift (photoz) and ≈ 54 per cent have spectroscopic redshift (specz). Hardness ratios ($\mathrm{HR} = \frac{\mathrm{H-S}}{\mathrm{H+S}}$, where H and S are the net counts of the sources in the hard and soft band, respectively) were estimated for all X-ray sources using the Bayesian estimation of hardness ratios method (BEHR; Park et al. 2006). The intrinsic column density, N_H, for each source was then calculated using its redshift and assuming an X-ray spectral power law with slope $\Gamma = 1.8$. This information is available in the catalogue presented in Marchesi et al. (2016).

We only use sources within both the COSMOS and UltraVISTA (McCracken et al. 2012) regions. UltraVISTA covers 1.38 deg^2 of the COSMOS field (Laigle et al. 2016) and has deep near-infrared (NIR) observations (*J*, *H*, K_s photometric bands) that allow us to derive more accurate host galaxy properties through SED fitting (see below). There are 1718 X-ray sources that lie within the UltraVISTA area of COSMOS. Out of these, 1073 satisfy the photometric criteria mentioned above, have reliable SED fits (see section 3.1) and meet the mass completeness requirements (see Section 3.4 in Mountrichas et al. 2022b).

The X-ray catalogue was cross-matched with the COSMOS photometric data set produced by the *Herschel* Extragalactic Legacy Project (HELP) collaboration (Shirley et al. 2019, 2021) to construct the SEDs of the X-ray sources and fit them to obtain measurements of the host galaxy properties. HELP includes homogeneous and calibrated multiwavelength data from 23 of the premier extragalactic survey fields imaged by the *Herschel* Space Observatory which form the HELP.

2.2 Boötes

We also use X-ray AGN observed by the *Chandra* X-ray Observatory within the 9.3 deg^2 Boötes field of the NOAO Deep Wide-Field Survey (NDWFS). The catalogue is compiled and fully described in Masini et al. (2020). It consists of 6891 X-ray point sources with an exposure time of about 10 ks per XMM pointing and a limiting flux of 4.7×10^{-16}, 1.5×10^{-16} and 9×10^{-16} erg cm^{-2} s^{-1}, in the $0.5 - 7$ keV, $0.5 - 2$ keV and 2–7 keV energy bands, respectively. A total of 2346 (∼ 33 per cent) of the X-ray sources in this catalogue have available spectroscopic redshifts (specz). For the remaining sources, we use hybrid photometric redshifts (photoz; Duncan et al. 2018b, a, 2019) that are available in the Masini et al. (2020) catalogue. The X-ray absorption of each X-ray AGN is available and is parameterized with N_H. N_H has been calculated from HR estimations, by applying the BEHR method. A fixed Galactic absorption of $N_{H,Gal} = 1.04 \times 10^{20}$ cm^{-2} is assumed. Mountrichas et al. (2021c) cross-matched the X-ray catalogue with the Boötes photometric catalogue produced by HELP to enrich the dataset with photometry

from optical to far-IR. The final X-ray Boötes sample used in our analysis consists of 1020 AGN.

2.3 eFEDS

In our analysis, we include X-ray AGN observed in the eFEDS field. The catalogue is presented in Brunner et al. (2022). eROSITA (extended ROentgen Survey with an Imaging Telescope Array; Predehl et al. 2021) is the primary instrument on the Spektrum–Roentgen–Gamma (SRG) orbital observatory (Sunyaev et al. 2021). SRG was built to provide a sensitive, wide-field-of-view X-ray telescope with improved capabilities compared to those of XMM-Newton and Chandra, the two most sensitive targeting X-ray telescopes in operation. The data set includes 27 910 X-ray sources detected in the 0.2–2.3 keV energy band with a flux limit of $\approx 7 \times 10^{-15}$ erg cm^{-2} s^{-1} in the 0.5 − 2.0 keV energy range. Details of the source detection are given in Brunner et al. (2022) (see their Section 3.3, Appendix A, and Fig. 3). In brief, their method is based on selecting source candidates according to the statistics of fitting source images with a point spread function (PSF-)convolved model. First, a preliminary catalogue is created that contains all the potential source candidates. Then, a background map is generated using the preliminary catalogue. Next, the preliminary catalogue is used as input to the PSF-fitting procedure, that selects reliable sources from this catalogue. By comparing the best-fit source model with a zero-flux (pure background) model, the algorithm calculates a detection likelihood L for each source, defined as $L = -\ln P$, where P is the probability of the source being caused by random background fluctuation. The final catalogue consists of sources detected above a detection likelihood of 6 in the most sensitive 0.2–2.3 keV band (see also fig. 5 in Salvato et al. 2022). Various criteria are applied to exclude problematic sources from our analysis (for a detail description see Section 2.1 in Mountrichas et al. 2022c). Furthermore, we restrict our sources to those within the KiDS + VIKING area (Kuijken et al. 2019; Hildebrandt et al. 2020). NIR photometry outside of this region is shallow which significantly affects the accuracy and reliability of the photoz calculations (Section 6.1 in Salvato et al. 2022). This area encompasses 10 294 extragalactic X-ray sources. Liu et al. (2022) performed a systematic X-ray spectral fitting analysis on all the X-ray systems, providing fluxes and luminosities — among other X-ray properties — for the eFEDS sources. We use their posterior median, intrinsic (absorption-corrected) X-ray fluxes in the 2–10 keV energy band.

Mountrichas et al. (2022c) restricted the X-ray catalogue to $0.5 < z < 1.5$. This was due to the unavailability of a large reference (non-AGN) sample at higher redshifts, with which they could compare the SFR of their AGN. In our analysis, we extend the X-ray catalogue to also include AGN at $1.5 < z < 2.5$, applying the same photometric and quality criteria as in Mountrichas et al. (2022c). We also select only X-ray sources that satisfy the mass completeness limits of the field at this redshift range, following the method of Pozzetti et al. (2010) (for more details see Section 3.4 in Mountrichas et al. 2022c). Our X-ray AGN catalogue consists of 2860 sources within a redshift range of $0.5 < z < 2.5$.

2.4 XMM-*XXL*

The XMM-Newton *XXL* survey (XMM-*XXL*; Pierre et al. 2016) is a medium-depth X-ray survey that covers a total area of 50 deg^2 split into two fields equal in size, the XMM-*XXL* North (XXL-N) and the XMM-*XXL* South (XXL-S). The *XXL*-N sample consists of 8445 X-ray sources. Of these X-ray sources, 5294 have SDSS counterparts and 2512 have reliable spectroscopy (Menzel et al. 2016; Liu et al. 2016). Mid-IR and near-IR was obtained following the likelihood ratio method (Sutherland & Saunders 1992) as implemented in Georgakakis & Nandra (2011). For more details on the reduction of the *XMM* observations and the IR identifications of the X-ray sources, see Georgakakis et al. (2017). The X-ray absorption of the AGN has been calculated in Masoura et al. (2021), by calculating the HR of the sources using the BEHR method (for details see Section 3.2 in Masoura et al. 2021). For those sources with no specz measurement, we use their photoz calculations presented in Masoura et al. (2018). For their estimation, a machine-learning technique has been applied (TPZ; Carrasco Kind & Brunner 2013), as described in Mountrichas et al. (2017), Ruiz et al. (2018).

In our analysis, we use the X-ray sample presented in Masoura et al. (2018). However, for consistency with the other X-ray data sets used in our analysis, we apply the same photometric criteria mentioned in Section 2 as well as the same quality criteria (see Section 3.1). Furthermore, we calculate the mass completeness limits of the field at the three redshift intervals used in our study and use only AGN that have M_* above these limits. For this purpose, we apply the method described in Pozzetti et al. (2010), utilizing equation (1) in Mountrichas et al. (2021c) and using the K band with $m_{lim} = 20.0$ mag (Georgakakis et al. 2017). Our calculations show that the mass completeness of the sample is defined at $\log[M_{*,95\ \mathrm{per\ centlim}}(M_\odot)] = 10.55, 11.00, 11.20$ at $0.5 < z < 1.0$, $1.0 < z < 1.5$ and $1.5 < z < 2.5$, respectively. Application of these criteria results in 686 X-ray AGN in *XXL*-N.

Table 1. Number of X-ray AGN that meet the photometric, quality, and mass completeness criteria (see text for more details) in each redshift interval.

Field	Total	$0.5 < z < 1.0$	$1.0 < z < 1.5$	$1.5 < z < 2.5$
Boötes	1020	590	298	132
COSMOS	1073	328	272	473
eFEDS	2860	1145	722	993
XMM-XXL-N	686	409	118	159
all fields	5639	2472	1410	1757

2.5 Final sample

Our final AGN data set consists of 5639 X-ray sources, covering a redshift range of $0.5 < z < 2.5$. Table 1 presents the number of sources in each field and redshift interval. Fig. 1 presents the intrinsic (absorption corrected) L_X distribution of the AGN used in this study. Our sources span more than three orders of magnitude in L_X. The eFEDS field contributes the majority of the luminous ($\log[L_{X,2-10\,\mathrm{keV}}(\mathrm{ergs}^{-1})] > 44$) sources used in our work, while most of the AGN in the COSMOS field are low-to-moderate luminosity. Fig. 2 presents the X-ray luminosity as a function of redshift, for the three redshift bins used in our analysis. In our analysis, we also split the X-ray sources into four M_* bins. Table 2, presents the number of sources in each M_* and redshift bin.

3 ANALYSIS

In this section, we describe the SED fitting analysis applied to calculate the AGN host galaxy properties and how this information is used to classify the systems that AGN reside into quiescent, star-forming, and starburst.

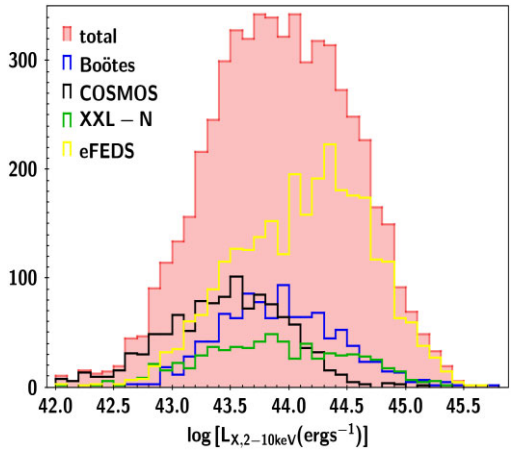

Figure 1. The intrinsic L_X distributions of the total sample used in our analysis (red-shaded area) and of AGN in the four individual fields. eFEDS has the most luminous AGN, whereas the COSMOS field consists, mainly, of low-to-moderate luminosity sources.

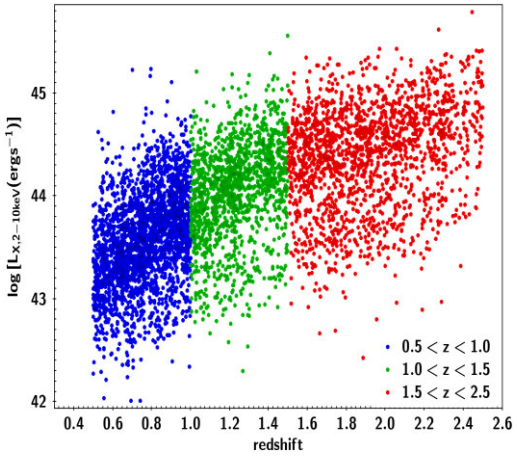

Figure 2. The intrinsic L_X as a function of redshift. The datapoints are colour-coded following the three redshift intervals used in our measurements.

Table 2. Number of X-ray AGN in each of the stellar mass and redshift bins used in our analysis.

log [M$_*$(M$_\odot$)]	Total	0.5 < z < 1.0	1.0 < z < 1.5	1.5 < z < 2.5
10.0 – 10.5	230	184	9	37
10.5 – 11.0	1299	809	282	208
11.0 – 11.5	2797	1165	757	875
11.5 – 12.0	1105	272	310	523

3.1 Spectral energy distribution fitting

The host galaxy properties of the AGN in the the Boötes, *COSMOS-Legacy*, and the eFEDS fields, have been measured in Mountrichas et al. (2021c), Mountrichas et al. (2022b), Mountrichas et al. (2022c), respectively, by applying SED fitting. For that purpose, the CIGALE algorithm (Boquien et al. 2019; Yang et al. 2020, 2022) has been utilized. CIGALE allows inclusion of the X-ray flux in the fitting process and has the ability to account for the extinction of the ultraviolet and optical emission in the poles of AGN (Yang et al. 2020; Mountrichas et al. 2021a; Buat et al. 2021).

The same templates and parameter space has been used to fit the AGN in the different data sets (Section 2). This minimizes any systematic effects that may be introduced due to the different modules and parametric grid used in the fitting process. As already noted, in the case of the *XXL*-N sources, we do not use the SFR and M_* measurements of Masoura et al. (2018). Instead, we have made new runs of CIGALE for these AGN, using the same SED fitting analysis, as for the other three fields.

A detailed description of the fitting process is provided in Mountrichas et al. (2021c), Mountrichas et al. (2022b), Mountrichas et al. (2022c). In brief, a delayed star formation history mode a function form SFR $\propto$ t $\times$ exp($-$t/τ) is used to fit the galaxy component. A star formation burst is included (Ciesla, Elbaz & Fensch 2017; Małek et al. 2018; Buat et al. 2019) as a constant ongoing period of star formation of 50 Myr. The Bruzual & Charlot (2003) single stellar population template is used to model the stellar emission. Stellar emission is attenuated following Charlot & Fall (2000). The dust heated by stars is modelled following Dale et al. (2014). The SKIRTOR template (Stalevski et al. 2012, 2016) is used for the AGN emission. The values for the various parameters of the SED fitting are similar for the AGN in all the four fields used in this work and are presented in Tables 1 in Mountrichas et al. (2021c), Mountrichas et al. (2022b), Mountrichas et al. (2022c).

To exclude sources that are badly fitted and have unreliable host galaxy measurements, we follow the criteria applied in previous studies (e.g. Mountrichas et al. 2021b, c; Buat et al. 2021; Mountrichas et al. 2022b, c). Specifically, we reject AGN with a reduced $\chi^2 > 5$. We also exclude sources for which CIGALE could not constrain their SFR and M_*. For that purpose, we use the two estimates that CIGALE provides for each galaxy property. One value is evaluated from the best-fit model and the other weighs all models allowed by the parametric grid, with the best-fit model having the heaviest weight (Boquien et al. 2019). A large difference between these two values indicates that the probability density function is asymmetric and a simple model for the errors is not valid. Thus, in our analysis we only keep sources with $\frac{1}{5} \leq \frac{\mathrm{SFR_{best}}}{\mathrm{SFR_{bayes}}} \leq 5$ and $\frac{1}{5} \leq \frac{\mathrm{M_{*,best}}}{\mathrm{M_{*,bayes}}} \leq 5$, where SFR$_{\rm best}$ and M$_{*,\rm best}$ are the best-fit values of SFR and M_*, respectively, and SFR$_{\rm bayes}$ and M$_{*,\rm bayes}$ are the Bayesian values estimated by CIGALE (e.g. Mountrichas et al. 2021b, c; Buat et al. 2021; Mountrichas et al. 2022b, c).

3.2 Classification of sources

To identify AGN host galaxies that are quiescent, we use the criterion presented in Mountrichas et al. (2021c), Mountrichas et al. (2022b), Mountrichas et al. (2022c). This criterion uses the distribution of the specific SFR (sSFR $= \frac{\mathrm{SFR}}{\mathrm{M_*}}$) of each data set, at different redshift intervals. These distributions present a lower, second peak at low sSFR values. The galaxies that populate these lower peaks are classified as quiescent. Systems that have sSFR that is 0.6 dex higher than the mean value of the data set are considered starburst (e.g. Rodighiero et al. 2011, 2015). The remaining of the AGN population is then classified as star-forming. To examine whether our results and conclusions, presented in the next sections, are sensitive to the classification method applied, we have also used different criteria for the AGN host galaxy classification. For instance, we identify as quiescent sources that have sSFR values 0.3 dex below the mean value and as SB systems that have 0.3 dex above the mean sSFR value. We confirm that our results and conclusion are not affected by the classification method applied.

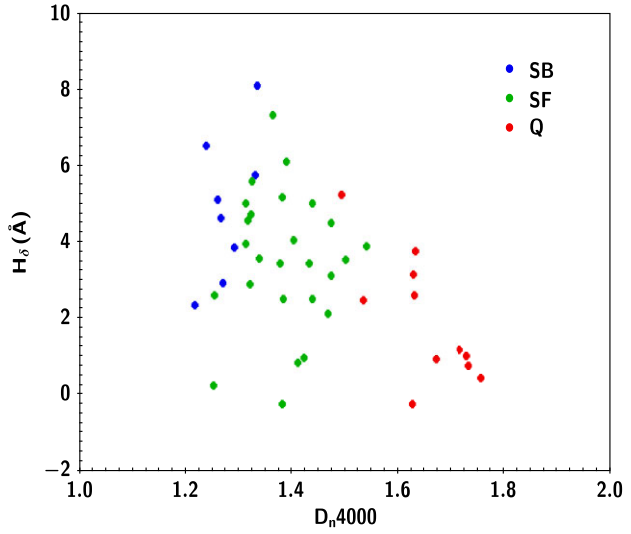

Figure 3. H_δ versus D_n4000 for the 52 of the X-ray AGN from our analysis that are also included in the LEGA-C catalogue. AGN hosted by SB galaxies have the youngest stellar populations (smallest D_n4000 values) and have experienced recent star formation bursts (high H_δ values). Q systems have the oldest stars (highest D_n4000 values) and present no signs of recent bursts (smallest H_δ values). AGN that live in SF galaxies have intermediate H_δ and D_n4000 values.

Furthermore, we examine whether our classification is consistent with the ages of the stellar populations of the AGN hosts. For that purpose, we use the information included in the Large Early Galaxy Astrophysics Census (LEGA-C) catalogue. The LEGA-C catalogue includes data obtained from the LEGA-C survey (van der Wel et al. 2021; Straatman et al. 2016). The third data release contains galaxy spectra for 3741 unique sources that cover a redshift range from 0.6 to 1.3. The sources lie within the UltraVISTA region of the COSMOS field. The catalogue includes measurements for two stellar age sensitive tracers, the equivalent width (EW) of Hδ absorption and the D_n4000 index (Worthey & Ottaviani 1997; Balogh et al. 1999). D_n4000 is small for young stellar populations and large for old, metal rich galaxies. The EW of H_δ rises rapidly in the first few hundred Myrs after a burst of star formation, when O- and B-type stars dominate the spectrum and then decreases when A-type stars fade (e.g. Kauffmann et al. 2003; Wu et al. 2018; Mountrichas et al. 2022a). We cross-match our X-ray dataset with the LEGA-C catalogue, using a radius of 1″and the optical coordinates provided in each catalogue. There are 52 AGN that are included in both catalogues, after applying several criteria to exclude sources with unreliable measurements (for more details see Section 2.2.3 in Mountrichas et al. 2022a). Our goal is to examine how our classified AGN host galaxies are distributed in the H_δ-D_n4000 space. This is shown in Fig. 3. AGN hosted by SB galaxies have the youngest stellar populations (smallest D_n4000 values) and have experienced (recent) star formation bursts (high H_δ values). Q systems have the oldest stars (highest D_n4000 values) and present no signs of recent bursts (smallest H_δ values). AGN that live in SF galaxies have intermediate H_δ and D_n4000 values. Although this subset is small, the results of this exercise indicate that the criteria we have applied to classify AGN host galaxies into SB, SF, and Q are robust.

Table 3 presents the number of Q, SB and SF galaxies that host X-ray AGN, in the three redshift intervals used in our analysis. Only sources with $10.0 < \log[M_*(M_\odot)] < 12.0$ are taken into consideration. As expected, the fraction of AGN hosted by SB galaxies increases as we move to higher redshifts while the fraction of quiescent systems increases at lower redshifts (e.g. Shimizu et al. 2015; Koutoulidis et al. 2022). However, the bulk of the accretion density of the Universe is associated with star-forming systems, at all redshift ranges probed by our sample, in agreement with previous studies (e.g. Georgakakis et al. 2014; Rodighiero et al. 2015). At $0.5 < z < 1.5$ the fraction of AGN hosted by quiescent systems is similar to that found by Mountrichas et al. (2021b) ($\sim$ 12 per cent, see their fig. 6). At higher redshifts ($1.5 < z < 2.5$) the fraction of quiescent galaxies that host AGN ($\sim$ 16 per cent) is consistent with that found by Rodighiero et al. (2015) ($\sim$ 11 per cent). Similar fractions of quiescent galaxies ($15-20$ per cent) has also been found in non-AGN systems (e.g. Fontana et al. 2009). Regarding, AGN hosted by SB galaxies, in our data set this fraction is significantly higher compared to that quoted by Rodighiero et al. (2015) ($\sim$ 30 per cent versus$\sim$ 6 per cent). Albeit, our sample spans significantly higher X-ray luminosities compared to theirs, in this redshift regime ($43.5 < \log[L_{X,2-10\,keV}(ergs^{-1})] < 45$ versus $41.8 < \log[L_{X,2-10\,keV}(ergs^{-1})] < 43.6$) and AGN that span such high X-ray luminosities have been associated with increased SFR compared to less luminous sources (e.g. Masoura et al. 2021; Mountrichas et al. 2021c, 2022c; Pouliasis et al. 2022).

Table 3. Number of X-ray AGN that live in Q, SF, and SB galaxies, in the three redshift intervals used in our analysis. Only AGN with $10.0 < \log[M_*(M_\odot)] < 12.0$ are included. In the parentheses we quote the fraction of each AGN population in the corresponding redshift interval.

	Total	$0.5 < z < 1.0$	$1.0 < z < 1.5$	$1.5 < z < 2.5$
SF	3575	1775 (73%)	920 (68%)	880 (53.5%)
SB	939	181 (7.5%)	261 (19%)	497 (30.3%)
Q	917	474 (19.5%)	177 (13%)	266 (16.2%)

4 RESULTS

In this section, we study the AGN accretion (L_X) and the L_X/SFR ratio as a function of stellar mass. All measurements presented are the median values of the properties in each bin. Bins that include less than 20 sources are excluded from our analysis. All errors presented have been calculated using a bootstrap resampling method (e.g. Loh 2008). We note that in our analysis only X-ray detected sources are included. Previous similar studies have also included undetected AGN in their measurements, by applying stacking analysis (e.g. Mullaney et al. 2012; Rodighiero et al. 2015; Yang et al. 2018). This allows to average the black hole growth rate over long time intervals. However, using only detected sources gives the advantage that the measured X-ray luminosities provide a tracer of black hole luminosity independent of the duty cycle (Carraro et al. 2022). In other words, the quantities we present below trace the average properties of the active population of galaxies at any given epoch.

4.1 L_X versus M_*

Fig. 4 presents the X-ray luminosity versus the host galaxy stellar mass, for SB, SF, and Q systems (blue squares, green circles, and red triangles, respectively), at different redshift intervals, as labeled at the top of each panel. We notice that SB systems showcase an increased median X-ray luminosity (and thus accretion rate) compared to SF galaxies, and Q galaxies show a deficit of L_X compared to SF systems, at similar M_*. This is in agreement with the results of previous

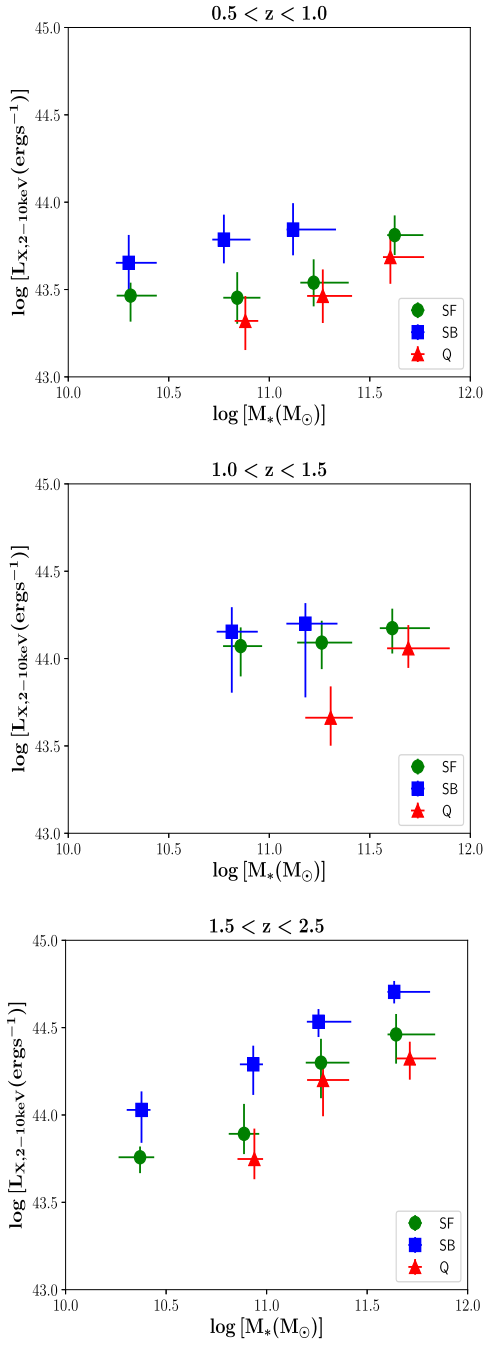

Figure 4. L_X as a function of M_*. The results are colour-coded based on the classification of the sources. Each panel corresponds to a different redshift interval. Errors have been calculated using bootstrap resampling. SB systems showcase an increased median L_X compared to SF galaxies and Q systems show a deficit of L_X compared to SF galaxies, at similar M_*. A mild increase of L_X (by ∼0.5 dex) with M_* is found for all AGN host galaxy classifications, at all redshifts spanned by our data set.

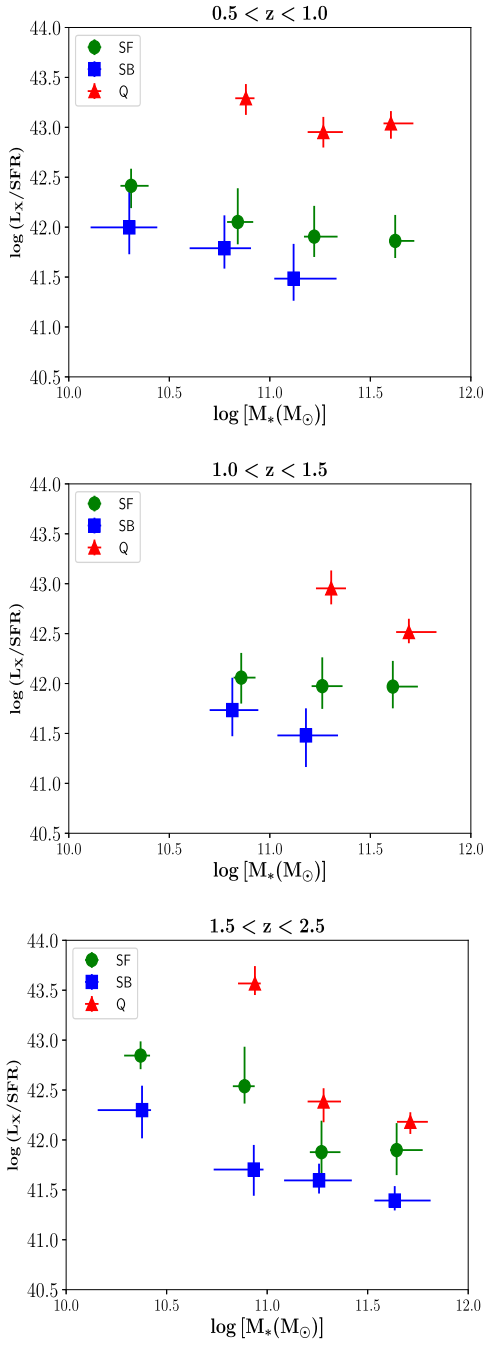

Figure 5. L_X/SFR as a function of M_*. The amplitude of L_X/SFR is higher for Q compared to SF and SB and presents only a weak dependence on stellar mass.

similar studies that attribute this behaviour, in conjunction with the SFR-M_* (MS) relation, to a gradual exhaustion of the gas that fuels both the SMBH and the SFR (e.g. Rodighiero et al. 2015), possibly accompanied by a proportional variation in Eddington ratios (e.g. Carraro et al. 2022).

Furthermore, L_X presents a mild increase (up to 0.5 dex) with M_*, in particular at high redshifts ($1.5 < z < 2.5$). We verified (Appendix A) that this trend is consistent in all four fields considered in this work. In COSMOS, our average $L_X - M_*$ relations generally follow similar patterns, but have lower normalizations (in line with Carraro et al. 2022, that used detected X-ray sources in COSMOS). This is because the COSMOS field is characterized by an L_X distribution skewed towards lower values (Fig. 1). Similar trends have also been found in previous studies (e.g. Mullaney et al. 2012; Rodighiero et al. 2015; Yang et al. 2018; Carraro et al. 2020, 2022), but a more direct comparison can be made with the results of Carraro et al. (2022) that used only the detected X-ray sources of the Carraro

et al. (2020) sample. They find a (mild) increase of L_X with M_*, similar to our results.

The increase of L_X with M_* we detect is most probably driven by the combined effect of the underlying slope of the $M_{BH} - M_*$ relation and the variation of the mean Eddington ratio $\lambda \propto L_X/M_*$ (Carraro et al. 2022). On the assumptions of a relatively constant $M_{BH} - M_*$ relation for AGN up to $z \sim 2$ (e.g. Suh et al. 2019), the gradual flattening and overall decrease of our $L_X - M_*$ with cosmic time, could be ascribed to a decrease of the underlying mean Eddington ratio, especially evident for the most massive galaxies allegedly hosting, on average, the most massive SMBHs. Indeed, as we show in Appendix B (Fig. B1), the increase in L_X with M_* at high redshift is mostly driven by the most luminous sources, a possible signature that SMBHs in the more massive galaxies tend to accrete at larger rates at earlier epochs.

4.2 L_X/SFR versus M_*

In Fig. 5, we plot the ratio log(L_X/SFR) as a function of M_*, for different redshift intervals, as labelled at the top of each panel. Our data suggest that SB have, at all redshifts explored here, a median L_X/SFR ratio a factor of ∼2–3 and ∼10 lower than SF and Q galaxies, respectively, with only a weak dependence on stellar mass. Previous studies have found either a positive correlation (Rodighiero et al. 2015; Yang et al. 2018; Carraro et al. 2020) or a flat relation (Mullaney et al. 2012) between log(L_X/SFR) (or BHAR/SFR) and M_*, with the caveat that these studies included stacked sources in their analysis. We also note that the amplitude of the log(L_X/SFR)-M_* relation in our results is about an order of magnitude higher than the amplitude presented in the aforementioned studies. This is mainly due to the inclusion, in our analysis, of X-ray sources detected in wide fields (eFEDS, XMM-*XXL*, Boötes), i.e. our sample includes a larger number of luminous AGN (Fig. 1). Furthermore, application of stacking analysis in these previous studies have allowed them to include very faint sources in their calculations. The different luminosities probed among our study and the previous works mentioned above, affect the amplitude of the log(L_X/SFR)-M_* relation, however, we do not expect to affect the overall trends (see Appendix B).

To examine if the observed trends in the log(L_X/SFR)-M_* relation are driven by L_X or SFR, in Fig. 6 we plot L_X versus SFR, for SF, SB, and Q AGN host galaxies, in the same redshift intervals as in the previous Figures. The median SFR increases by a large factor (up to 3.5 dex) across M_*, when moving from Q to SB galaxies. The corresponding increase of the mean L_X is significantly smaller (∼0.7 dex), at all redshift intervals and for all AGN host galaxy classifications. We thus conclude that the strong increase observed in the L_X/SFR ratio from SB to Q at fixed M_* is mostly driven by a significant drop in SFR.

In Appendix B, we explore the log(L_X/SFR) as a function of M_*, for luminous and low to moderate L_X AGN. Similar trends are found for both AGN populations (Fig. B2). Luminous AGN have higher log(L_X/SFR) amplitude compared to less luminous X-ray sources, at low redshifts. However, this picture reverses, for AGN hosted by Q galaxies, at the highest redshift interval spanned by our data set. This behaviour is due to how the L_X and SFR vary as a function of M_* for the different AGN host galaxy classifications and for different L_X and redshifts (for more details see Appendix B).

We conclude that our results show that Q systems present the highest amplitude in the log(L_X/SFR)-M_* relation due to their lowest SFRs, while SB galaxies have the smallest log(L_X/SFR) ratio due to their highest SFRs.

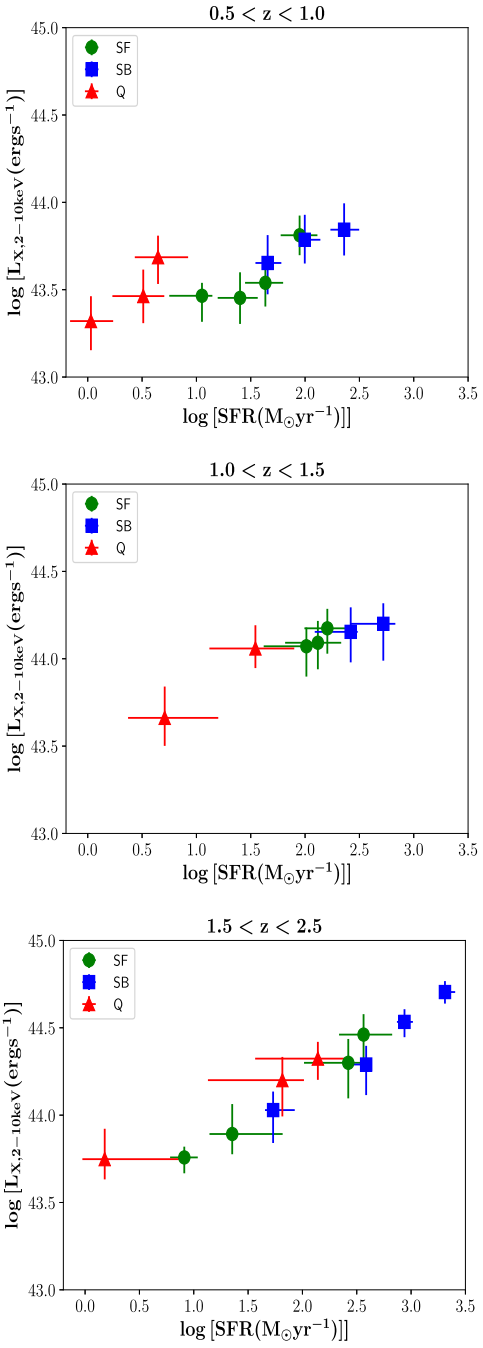

Figure 6. L_X as a function of SFR for SB, SF, and Q AGN host galaxies, at three redshift intervals. At all redshift ranges, L_X increases by a smaller factor compared to the increase of SFR.

5 DISCUSSION

As anticipated in Section 1, studying AGN statistical samples averaged in bins of stellar mass, SFR and L_X, provides clues to the overall connection among these properties, but it does not necessarily provide insight into the actual evolutionary phases, if any, between the starburst and star forming/quiescent phases. To extract possible evolutionary sequences characterising AGN galactic hosts, we need to connect the Lx and SFR of SB, SF and Q into a time sequence, and check whether such sequences are comparable to predictions from theoretical models (e.g. Rodighiero et al. 2015). To this purpose,

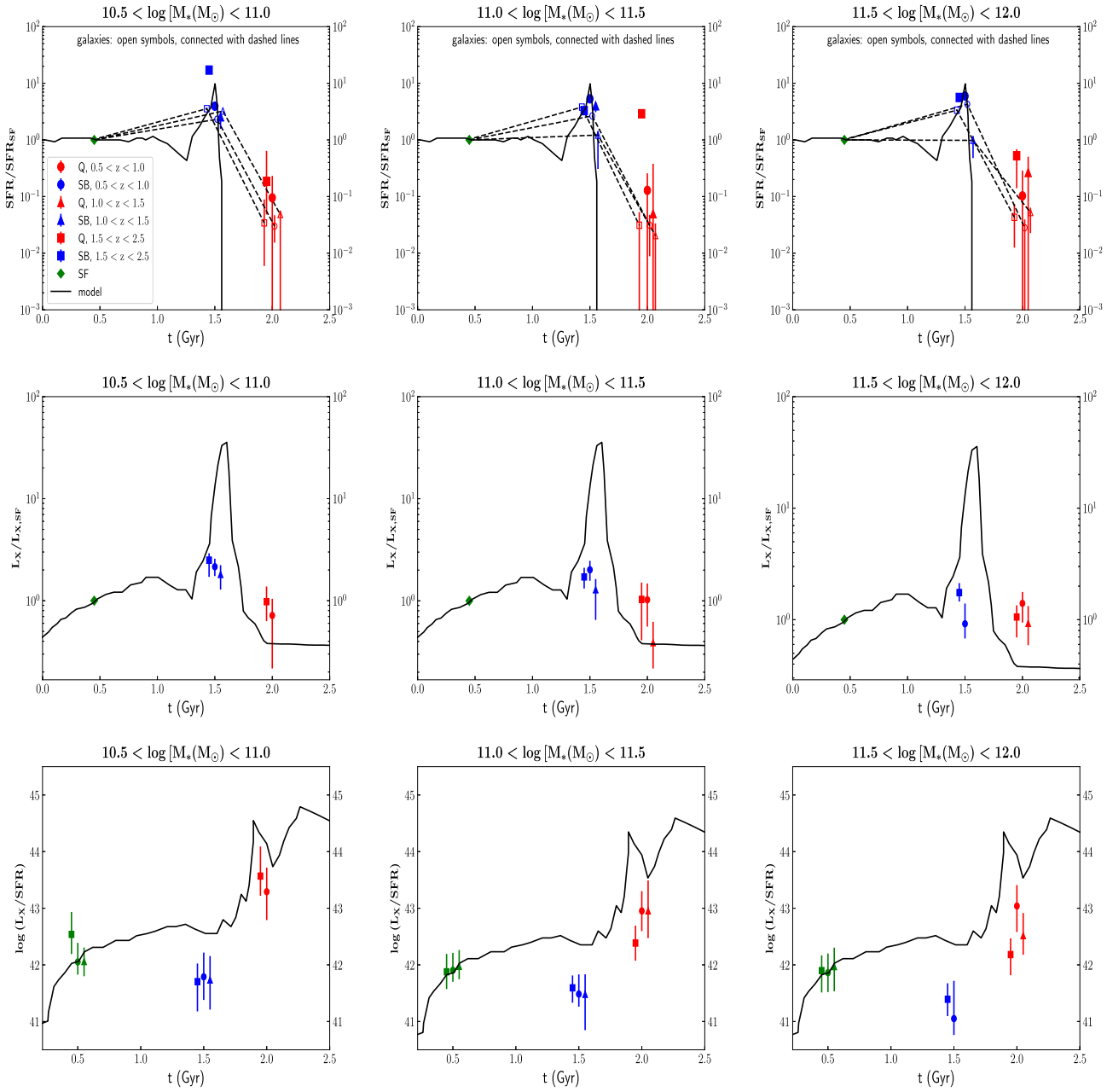

Figure 7. Evolution of SFR (top panels), L_X (middle panels), and their ratio logL_X/SFR (bottom panels) with time. Each row corresponds to a different M_* interval, as indicated as the top of each plot. Filled symbols present the results for galaxies that host X-ray AGN. Open symbols connected with dashed lines show the results for non-AGN galaxies (top panels). The black lines present the predictions of hydrodynamical models that follow the black hole growth and the star formation during a galaxy merger (Di Matteo et al. 2005; Hopkins 2012).

in this Section, we study how the L_X/SFR ratio varies along the different phases of the galaxy, from the SF to the SB and Q phases, and compare our observations with theoretical light curves from SMBH-galaxy evolutionary models.

5.1 Evolution of L_X/SFR at different galaxy evolutionary sequences

We start by examining how the L_X/SFR evolves as the galaxy 'transits' from one phase to the other. We assume that the (host) galaxy is initially in a star forming phase. Then, the galaxy merges with another galaxy and the gas is converted to stars in intense bursts of star formation (SB phase), ∼1.5 Gyr later. Finally, when nearly all the gas has been depleted, the galaxy enters the Q state (at ∼2 Gyr) (e.g. Di Matteo et al. 2005). The transition times associated to each phase have been chosen on the assumption that these mirror those suggested by theoretical models, which are, in a typical binary merger scenario at z ∼ 1 − 2, ∼1 Gyr between the SB and SF phases and 0.5 Gyr between the SF and Q phase (e.g. Di Matteo et al. 2005; Springel et al. 2005; Hopkins 2012).

In Fig. 7, the top, middle and bottom panels show, respectively, the putative evolution of the SFR, L_X and the L_X/SFR ratio, when the galaxy 'transits' from the SF to the SB and then to the Q phase, assuming that these are correlated to each other. The results for

different M_* selections are presented, as indicated in the top of each panel. We do not show results for the lowest stellar mass bin ($10 < \log[M_*(M_\odot)] < 10.5$), since there are not enough Q AGN host galaxies in this M_* bin in our sample to allow robust calculations. The estimated median quantities reported are largely independent of the exact cuts in redshift and/or stellar mass interval chosen, and still hold true when assuming some evolution in the host galaxy stellar mass, following semi-empirical models, as discussed in the next section. We start discussing the bottom panels of Fig. 7, where we show that the L_X/SFR tends to gradually increase by up to $\sim 1 - 1.5$ dex when the host galaxy becomes Q.

To examine what drives the variation of the L_X/SFR with time, in the top and middle panels of Fig. 7, we normalize the SFR and the L_X, respectively, to the SFR and L_X of the SF (main sequence) galaxies and study them as a function of time. Both SFR and L_X increase as the galaxy moves from the SF to the SB and then decrease in the Q state. We find that the SFR increases by nearly an order of magnitude in the transition from the SF to the SB stage and then drops by almost two orders of magnitude from the SB to the Q phase. On the other hand, L_X increases by, only, up to a factor of two in the SB phase and then, in the Q phase, drops to similar values with those observed for SF galaxies. These results suggest that the L_X/SFR fluctuations we observe during the different galaxy evolutionary sequences are largely driven by variations in the SFR. It is also interesting to note that the aforementioned fluctuations of SFR and L_X are nearly independent of both redshift and galaxy stellar mass.

Our next step is to compare our inferred SFR evolutionary tracks with those from galaxies not detected as AGN. Mountrichas et al. (2021c), Mountrichas et al. (2022b), Mountrichas et al. (2022c) constructed galaxy control samples applying the same photometric requirements and SED fitting techniques (same templates and parameter values) as in the X-ray sources adopted in this work. Non-X-ray AGN systems have also been excluded from the control sample (for more details see Section 3.3 in e.g. Mountrichas et al. 2022c). We, thus, combine the galaxies from the Mountrichas et al. datasets and compile a sample of $\sim$130, 000 sources within the mass completeness limits, and similarly classify these galaxies into SB, SF and Q, following the same method as for the X-ray AGN (see Section 3.2). We then normalize the SFR of each class based on the SFR of the SF galaxies. The results are shown in the top panels of Fig. 7 (open symbols connected with dashed lines), for different M_* regimes. We find that for non-AGN sources the SFR increases in the SB phase and drops in the Q stage in a similar manner as for the X-ray AGN. The similarity in the variation of SFR from SB to Q galaxies between AGN and non-AGN galaxies, suggest that the AGN has a negligible impact on the quenching. Theoretical studies have suggested that the apparent lack of a (inverse) correlation between AGN activity and SFR found in observational works, could be induced by the different timescales characterizing the two processes (e.g. Hickox et al. 2014; Ward et al. 2022). Theoretical models indeed suggest that a delay of a few millions of years is required for the impact of a single episode of nuclear activity to have a measurable effect on star formation. The presence of such delays may explain, at least in part, why all galaxies of similar stellar mass in our sample share similar drops of the SFR from the SB/SF to the Q state, irrespective of their AGN activity. In other words, the combination of a delay and of relative short AGN lifetimes (e.g. Martini 2004; Shankar et al. 2004), could both contribute to wash out causal links between AGN luminosities and host galaxies SFR.

Another viable solution could be to start from a SB phase, on the assumption that the galaxy is forming out of the cooling of pristine gas clouds, and then gradually converts into a SF and finally into a Q phase (e.g. Granato et al. 2004, 2006; Lapi et al. 2006, 2018). Although, without clear age and structural discriminators, our current data cannot safely distinguish between these two evolutionary routes, our measurements presented in Fig. 4, suggest that SB could be the starting phase in a galaxy's lifetime.

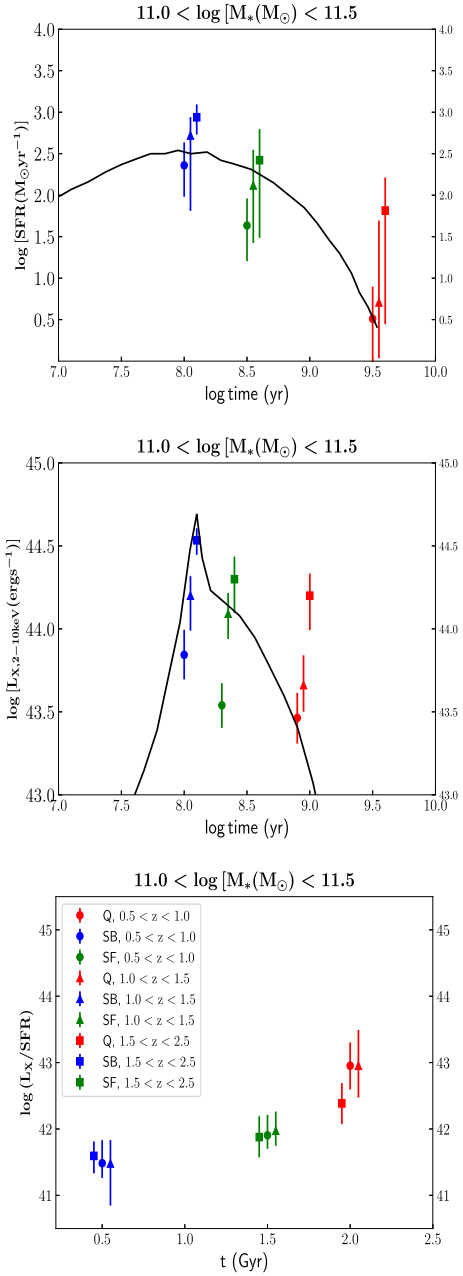

Figure 8. Evolution of SFR (top panel), L_X (middle panel), and their ratio $\log L_X$/SFR (bottom panel) with time, for AGN host galaxies with $11.0 < \log[M_*(M_\odot)] < 11.5$. In this exercise, we assume that the galaxy starts its life in a SB phase and then it enters the SF and finally becomes Q. The black lines show the predictions of the model presented in Granato et al. 2004. The x-axis in the top and middle panels, present the galactic age (in log), as shown in Figs. 2 and 3 in Granato et al. (2004).

In Fig. 8, we plot the SFR (top panel), the L_X (middle panel) and their ratio L_x/SFR (bottom panel), as a function of time, for AGN host galaxies with $11.0 < \log[M_*(M_\odot)] < 11.5$, assuming that the galaxy starts its life in a SB phase. The x-axis in the top and middle panels present the galactic age (in log) to allow us to compare our

observational measurements with the theoretical model of Granato et al. (2004) (see next Section). Similarly to the results presented above, the L_X/SFR ratio increases by up to $\sim 1 - 1.5$ dex when the host galaxy becomes Q. Both the SFR and L_X drop as the galaxy evolves from the SB to the SF and then the Q phase. This decrease is higher for SFR ($\sim$2 dex) compared to L_X ($\sim$1 dex). Similar results are found for the other stellar mass bins.

5.2 Comparison with theoretical predictions

To set the stage between our data and theoretical models, we follow Rodighiero et al. (2015) and compare in Fig. 7 our empirical renditions of AGN light curves with those extracted from hydrodynamic simulations inclusive of AGN feedback (Di Matteo et al. 2005; Hopkins 2012) We take the typical light curve of a galaxy hosted in a dark matter halo of 160 km/s (black lines in fig. 3 of Rodighiero et al. 2015).[1] The empirical light curves suggest that the AGN luminosity increases only by a factor of a few from the SF to the SB phase, and a similar drop is observed in the Q phase. This behaviour is not entirely aligned with what predicted by models which suggest that during the growth phase the BH grows by a factor of $>100 - 1000$ depending on the assumed initial BH seed. We also checked, via Monte Carlo simulations, that typical random measurement errors of 0.5 Gyr in galaxy ages and of 0.15 dex in X-ray luminosities, are not capable to wash out the peak of the AGN light curve and to reconcile data with models, thus suggesting that this discrepancy we observe between predicted and observed AGN X-ray light curves is robust.

On the other hand, the SFR is observed to actually behave as predicted, with an increase of a factor of a few up to an order of magnitude, followed by a drop of two orders of magnitudes, similar to what expected in AGN feedback models where an AGN wind is expelling mass from the host galaxy or at least injecting energy/momentum thus decreasing the possibility for any further gas fragmentation.

In Fig. 8, we assume instead that a galaxy starts its life in a SB phase and compare our observational measurements with the predictions of the model presented in Granato et al. (2004). We find even in this case that the SFR evolves from the SB to the SF and then to the Q phase, as predicted (top panel of Fig. 8). However, L_X (middle panel of Fig. 8) drops by $\sim$0.5 dex, compared to 1.5 dex predicted by the theoretical model. However, including observational uncertainties may improve the match to the models in this second type of models, at least at intermediate redshifts.

Taking these results at face value, we would conclude that in order to achieve a condition where the AGN luminosity drops only by a factor of a few from the peak whilst the SFR decreases significantly, a high AGN feedback efficiency and/or coupling with the interstellar medium (ISM) should be characterising AGN feedback processes.

The relatively limited pre-peak increase in the AGN luminosity, and to a lesser extent in our SFRs, observed in our data, may signal the fact that in our samples the SF and SB phases are close to each other. In addition, if our simulations inclusive of observational errors, are not able to resolve the tension in the discrepancy between predicted and observed AGN light curves, at least for some models (e.g. Springel et al. 2005; Hopkins et al. 2006), then it would imply that the post-peak phase of the AGN light curve does not decrease as sharply as predicted by some models, and this is in fact what seen by e.g. Lapi et al. (2014) to reproduce their FIR galaxy light curves, and also by some continuity equation models that require extended light curves (e.g. Shankar, Weinberg & Miralda-Escudé 2013; Aversa et al. 2015).

Interestingly, we find that for each of our galaxy classes, the increase in X-ray AGN luminosity is always smaller than the one in SFR within the same time lag, and in the SB the X-ray luminosity is nearly constant, despite the SFR still increasing by nearly an order of magnitude. Again, this behaviour in our data is not entirely paralleled especially in the merger models, which could either be a consequence of selection effect and/or observational errors, but also it could reflect the fact that the BH has reached a self-regulated state which prevents further substantial growth.

We note that all our results discussed above remain valid under the assumption that the stellar mass does not grow more than a factor of $\sim$2 within the timeframe considered, i.e. $\sim$2 Gyr, or even by following back in time the stellar progenitors. We checked in fact that by selecting the SF and SB progenitors of the quiescent galaxies of a given chosen M_* following, e.g. the average stellar mass growth histories of Moster, Naab & White (2018), or even Grylls et al. (2019), Behroozi et al. (2019) (see fig. 3 in Shankar et al. 2020), we find very similar results for the L_X, SFR evolution with time as the ones reported in Fig. 7.

6 CONCLUSIONS

We used $\sim$5500 X-ray AGN detected in four fields, namely the *COSMOS-Legacy*, the Boötes, the XMM-*XXL* and the eFEDS fields. The X-ray sources span a redshift range of $0.5 < z < 2.5$ and about three orders of magnitude in X-ray luminosity ($42.0 < \log[L_{X,2-10\,keV}(ergs^{-1})] < 45$), while their stellar mass ranges from $10.0 < \log[M_*(M_\odot)] < 12.0$. These sources meet strict photometric selection requirements and various selection criteria have been applied to ensure that only sources with robust host galaxy measurements are included in the analysis. The latter have been calculated via SED fitting, using the CIGALE code. Furthermore, our final sample consists only of AGN that satisfy the mass completeness limits of the field they belong. The X-ray sources are then classified into three classes, based on the star formation activity of the host galaxy, i.e. SF, SB and Q. For the classification, the sSFR of each system was used. Our final X-ray sample, consists of 3575 SF galaxies, 939 SB and 917 Q systems. The fraction of each class depends on the redshift, but at all redshift ranges used in our analysis, the bulk of the black hole accretion occurs in SF systems. Our main results can be summarised as follows:

(i) We found that SB systems have increased AGN accretion (L_X) compared to SF systems, at similar M_*. Q galaxies present the lowest L_X among the three classifications. We also find a mild increase of L_X with M_*, possibly related to a decrease of Eddington ratio with increasing stellar mass and at fixed $M_{BH} - M_*$ slope (e.g. Carraro et al. 2022). Our results also show a gradual flattening and overall decrease with cosmic time of the L_X at fixed M_*, which suggests a decrease of the underlying mean Eddington ratio, in particular for the most massive galaxies.

(ii) The amplitude of the L_X/SFR ratio is higher for Q systems compared to SF and SB galaxies. We also find that the L_X/SFR-M_* relation is nearly flat, in particular for the most massive galaxies.

(iii) The ratio of L_X/SFR decreases by $\sim$0.5 dex when the galaxy enters the SB phase and then increases by almost an order of magnitude in the Q phase. This variation is mostly driven by

[1] Our results would be similar for other choices of dark matter haloes. As shown by Rodighiero et al. (2015), in fact, light curves in larger haloes are predicted to be very similar.

variations in the SFR, whilst the L_X remains roughly constant from the SF to the SB and the Q states.

(iv) The fluctuation of SFR is consistent with what predicted by theoretical models, whereas the behaviour of L_X is not in line with merger models that predict an increase of L_X by a factor of $>100-1000$ in the SB phase.

(v) We also study the evolution of SFR for a galaxy control sample of non-AGN systems and found that it is very similar to that of X-ray AGN. This similarity in the variation of SFR between the two populations may suggest that AGN have a negligible impact on the star formation quenching or that the two processes proceed on different timescales.

ACKNOWLEDGEMENTS

GM acknowledges support by the Agencia Estatal de Investigación, Unidad de Excelencia María de Maeztu, ref. MDM-2017-0765. FS acknowledges partial support from the European Union's Horizon 2020 research and innovation programme under the Marie Skłodowska-Curie grant agreement No. 860744.

DATA AVAILABILITY

The data underlying this article will be shared on reasonable request to the corresponding author.

REFERENCES

Aird J., Coil A. L., Kocevski D. D., 2022, MNRAS, 515, 4860
Aversa R., Lapi A., de Zotti G., Shankar F., Danese L., 2015, ApJ, 810, 74
Balogh M. L., Morris S. L., Yee H. K. C., Carlberg R. G., Ellingson E., 1999, ApJ, 527, 54
Behroozi P., Wechsler R. H., Hearin A. P., Conroy C., 2019, MNRAS, 488, 3143
Bernardi M., Sheth R. K., Tundo E., Hyde J. B., 2007, ApJ, 660, 267
Boquien M., Burgarella D., Roehlly Y., Buat V., Ciesla L., Corre D., Inoue A. K., Salas H., 2019, A&A, 622, A103
Brunner H. et al., 2022, A&A, 661, A1
Bruzual G., Charlot S., 2003, MNRAS, 344, 1000
Buat V., Ciesla L., Boquien M., Małek K., Burgarella D., 2019, A&A, 632, A79
Buat V. et al., 2021, A&A, 654, A93
Carraro R. et al., 2020, A&A, 642, A65
Carraro R., Shankar F., Allevato V., Rodighiero G., Marsden C., Arévalo P., Delvecchio I., Lapi A., 2022, MNRAS, 512, 1185
Carrasco Kind M., Brunner R. J., 2013, MNRAS, 432, 1483
Charlot S., Fall S. M., 2000, ApJ, 539, 718
Ciesla L., Elbaz D., Fensch J., 2017, A&A, 608, A41
Civano F. et al., 2016, ApJ, 819, 62
Dale D. A., Helou G., Magdis G. E., Armus L., Díaz-Santos T., Shi Y., 2014, ApJ, 784, 83
DeBuhr J., Quataert E., Ma C.-P., 2012, MNRAS, 420, 2221
Di Matteo T., Springel V., Hernquist L., 2005, Nature, 433, 604
Duncan K. J., Jarvis M. J., Brown M. J. I., Röttgering H. J. A., 2018a, MNRAS, 477, 5177
Duncan K. J. et al., 2018b, MNRAS, 473, 2655
Duncan K. J. et al., 2019, A&A, 622, A3
Ferrarese L., Merritt D., 2000, ApJ, 539, 9
Fontana A. et al., 2009, A&A, 501, 15
Georgakakis A., Nandra K., 2011, MNRAS, 414, 992
Georgakakis A., et al., 2014, MNRAS, 443, 3327
Georgakakis A., Aird J., Schulze A., Dwelly T., Salvato M., Nandra K., Merloni A., Schneider D. P., 2017, MNRAS, 471, 1976
Graham A. W., 2016, in Galactic Bulges, Astrophysics and Space Science Library, Vol. 418. Springer International Publishing, Switzerland, p. 263
Granato G. L., Zotti G. D., Silva L., Bressan A., Danese L., 2004, ApJ, 600, 580
Granato G. L., Silva L., Lapi A., Shankar F., Zotti G. D., Danese L., 2006, MNRAS, 368, L72
Grylls P. J., Shankar F., Zanisi L., Bernardi M., 2019, MNRAS, 483, 2506
Habouzit M. et al., 2021, MNRAS, 503, 1940
Habouzit M. et al., 2022, MNRAS, 511, 3751
Hickox R. C., Mullaney J. R., Alexander D. M., Chen C.-T. J., Civano F. M., Goulding A. D., 2014, ApJ, 782, 11
Hildebrandt H. et al., 2020, A&A, 633, A69
Hopkins P. F., 2012, MNRAS, 420, L8
Hopkins P. F., Hernquist L., Cox T. J., Matteo T. D., Robertson B., Springel V., 2006, ApJS, 163, 1
Kauffmann G. et al., 2003, MNRAS, 341, 54
Komatsu E. et al., 2011, ApJS, 192, 18
Koutoulidis L., Mountrichas G., Georgantopoulos I., Pouliasis E., Plionis M., 2022, A&A, 658, A35
Kuijken K. et al., 2019, A&A, 625, A2
Laigle C. et al., 2016, ApJS, 224, 24
Lapi A., Shankar F., Mao J., Granato G. L., Silva L., Zotti G. D., Danese L., 2006, ApJ, 650, 42
Lapi A., Raimundo S., Aversa R., Cai Z.-Y., Negrello M., Celotti A., Zotti G. D., Danese L., 2014, ApJ, 782, 69
Lapi A. et al., 2018, ApJ, 857, 22
Liu Z. et al., 2016, MNRAS, 459, 1602
Liu T. et al., 2022, A&A, 661, A5
Loh J. M., 2008, ApJ, 681, 726
Magorrian J., et al., 1998, AJ, 115, 2285
Małek K. et al., 2018, A&A, 620, A50
Marchesi S. et al., 2016, ApJ, 817, 34
Martini P., 2004, cbhg, symp, p. 169M
Masini A. et al., 2020, ApJS, 251, 2
Masoura V. A., Mountrichas G., Georgantopoulos I., Ruiz A., Magdis G., Plionis M., 2018, A&A, 618, 31
Masoura V. A., Mountrichas G., Georgantopoulos I., Plionis M., 2021, A&A, 646, A167
McCracken H. J. et al., 2012, A&A, 544, A156
Menzel M.-L., et al., 2016, MNRAS, 457, 110
Moster B. P., Naab T., White S. D. M., 2018, MNRAS, 477, 1822
Mountrichas G., Corral A., Masoura V. A., Georgantopoulos I., Ruiz A., Georgakakis A., Carrera F. J., Fotopoulou S., 2017, A&A, 608, 39
Mountrichas G., Buat V., Yang G., Boquien M., Burgarella D., Ciesla L., 2021a, A&A, 646, A29
Mountrichas G., Buat V., Georgantopoulos I., Yang G., Masoura V. A., Boquien M., Burgarella D., 2021b, A&A, 653, A70
Mountrichas G., Buat V., Yang G., Boquien M., Burgarella D., Ciesla L., Malek K., Shirley R., 2021c, A&A, 653, A74
Mountrichas G. et al., 2022a, A&A, 667, 145
Mountrichas G., Masoura V. A., Xilouris E. M., Georgantopoulos I., Buat V., Paspaliaris E.-D., 2022b, A&A, 661, A108
Mountrichas G., Buat V., Yang G., Boquien M., Burgarella D., Ciesla L., Malek K., Shirley R., 2022c, A&A, 663, A130
Mullaney J. R. et al., 2012, ApJ, 753, L30
Park T., Kashyap V. L., Siemiginowska A., van Dyk D. A., Zezas A., Heinke C., Wargelin B. J., 2006, ApJ, 652, 610
Pierre M., et al., 2016, A&A, 592, 1
Pouliasis E. et al., 2022, A&A, 667, 56
Pozzetti L., et al., 2010, A&A, 523, 23
Predehl P. et al., 2021, A&A, 647, A1
Reines A. E., Volonteri M., 2015, ApJ, 813, 82
Rodighiero G. et al., 2011, ApJ, 739, L40
Rodighiero G. et al., 2015, ApJ, 800, L10
Ruiz A., Corral A., Mountrichas G., Georgantopoulos I., 2018, A&A, 618, A52

Salvato M. et al., 2022, A&A, 661, A3
Scoville N., et al., 2007, ApJS, 172, 1
Shankar F., Salucci P., Granato G. L., Zotti G. D., Danese L., 2004, MNRAS, 354, 1020
Shankar F., Weinberg D. H., Miralda-Escudé J., 2013, MNRAS, 428, 421
Shankar F. et al., 2016, MNRAS, 460, 3119
Shankar F., Bernardi M., Sheth R. K., 2017, MNRAS, 466, 4029
Shankar F. et al., 2019, MNRAS, 485, 1278
Shankar F. et al., 2020, MNRAS, 493, 1500
Shimizu T. T., Mushotzky R. F., Meléndez M., Koss M., Rosario D. J., 2015, MNRAS, 452, 1841
Shirley R. et al., 2019, MNRAS, 490, 634
Shirley R. et al., 2021, MNRAS, 507, 129
Springel V., et al., 2005, nat, 435, 629
Stalevski M., Fritz J., Baes M., Nakos T., Popović L. Č., 2012, MNRAS, 420, 2756
Stalevski M., Ricci C., Ueda Y., Lira P., Fritz J., Baes M., 2016, MNRAS, 458, 2288
Straatman C. M. S. et al., 2016, ApJ, 830, 51
Suh H. et al., 2019, ApJ, 872, 168
Suh H., Civano F., Trakhtenbrot B., Shankar F., Hasinger G., Sanders D. B., Allevato V., 2020, ApJ, 889, 32
Sunyaev R. et al., 2021, A&A, 656, 132
Sutherland W., Saunders W., 1992, MNRAS, 259, 413
van der Wel A. et al., 2021, ApJS, 256, 44
Ward S. R., Harrison C., Costa T., Mainieri V., 2022, MNRAS, 514, 2936
Worthey G., Ottaviani D. L., 1997, ApJS, 111, 377
Wu P.-F. et al., 2018, ApJ, 855, 85
Yang G. et al., 2018, MNRAS, 475, 1887
Yang G., Brandt W. N., Alexander D. M., Chen C.-T. J., Ni Q., Vito F., Zhu F.-F., 2019, MNRAS, 485, 3721
Yang G. et al., 2020, MNRAS, 491, 740
Yang G. et al., 2022, ApJ, 927, 192
Zinn P.-C., Middelberg E., Norris R. P., Dettmar R.-J., 2013, ApJ, 774, 66
Zubovas K., Nayakshin S., King A., Wilkinson M., 2013, MNRAS, 433, 3079

APPENDIX A: L_X VERSUS M_* IN DIFFERENT FIELDS

In this section, we examine the $L_X - M_*$ relation separately in each one of the fields, used in our analysis. Our goal is to check whether the measurements in each field are compatible with each other. For this exercise, we have used sources at $0.5 < z < 1.0$ since in this redshift range our data sets have the largest number of available sources (Table 1).

In Fig. A1, we present the L_X as a function of M_* for the Boötes, COSMOS, eFEDS, and XMM-*XXL* fields, for AGN hosted by SF, SB, and Q galaxies. Based on the results, the measurements are consistent among the various field. COSMOS has lower L_X values, for all three classifications, but this is expected since the vast majority of X-ray AGN in this field have low to moderate luminosity sources ($\log[L_{X,2-10\,keV}(ergs^{-1})] < 44$, Fig. 1). Most importantly, the trends observed are similar in all four fields. Therefore, we conclude that the four fields give consistent results with each other.

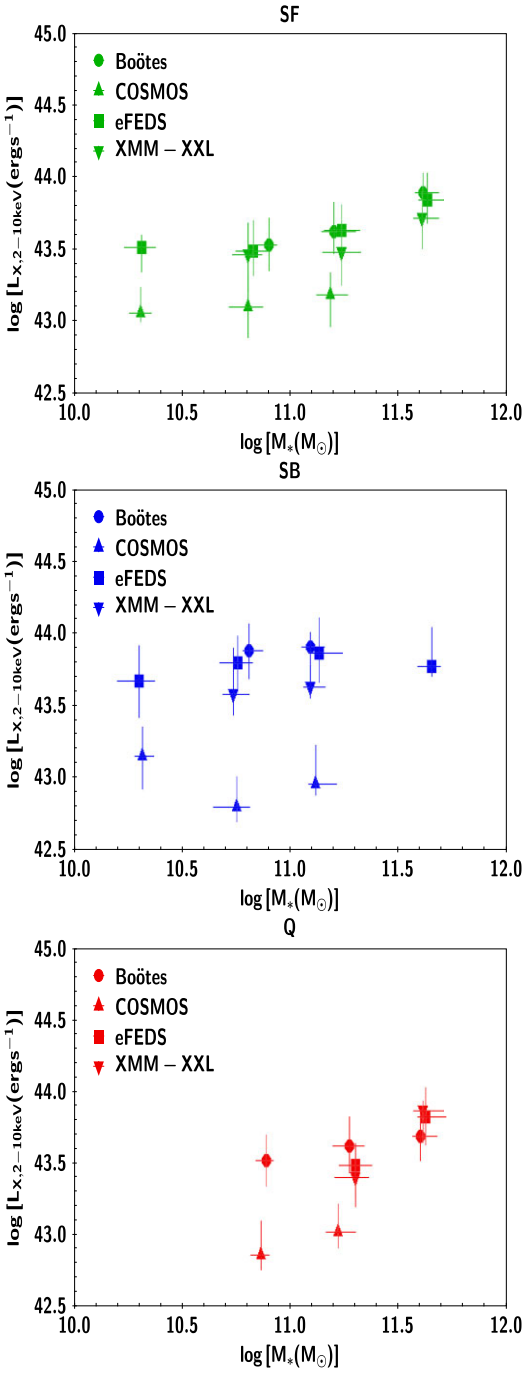

Figure A1. L_X versus M_* at each field separately, for sources with $0.5 < z < 1.0$. All fields give consistent results within the same redshift, L_X and M_* bins. COSMOS L_X measurements are by ∼0.5 dex lower, as expected from the L_X distribution of AGN in this field. Most importantly, the observed trends are similar between the four fields.

APPENDIX B: DEPENDENCE ON L_X

In this section, we examine if the observed trends of L_X and the ratio L_X/SFR as a function of M_*, presented in Sections 4.1 and 4.2, are different between low to moderate L_X ($\log[L_{X,2-10\,keV}(ergs^{-1})] < 44$) and high L_X AGN ($\log[L_{X,2-10\,keV}(ergs^{-1})] > 44$).

Fig. B1 presents the $L_X - M_*$ relation for the two AGN populations. The (mild) increase of L_X with M_* seems to be mainly driven by the most luminous X-ray sources.

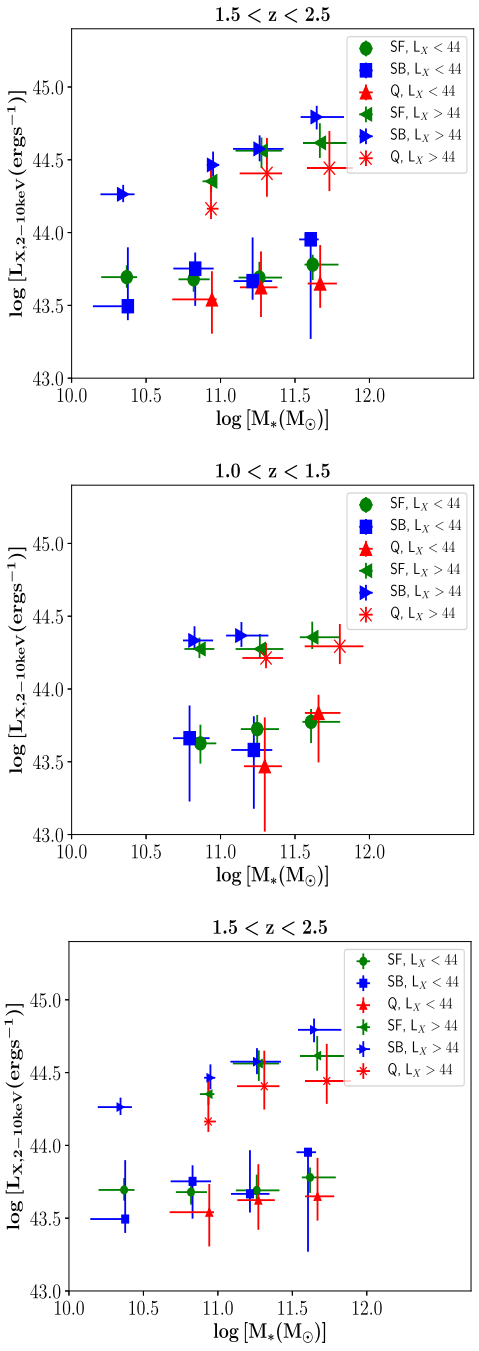

Figure B1. L_X as a function of M_*, for AGN with $\log[L_{X,2-10\,keV}(ergs^{-1})] > 44$ and $\log[L_{X,2-10\,keV}(ergs^{-1})] < 44$. The mild increase of L_X with M_* is mostly driven by the most luminous sources.

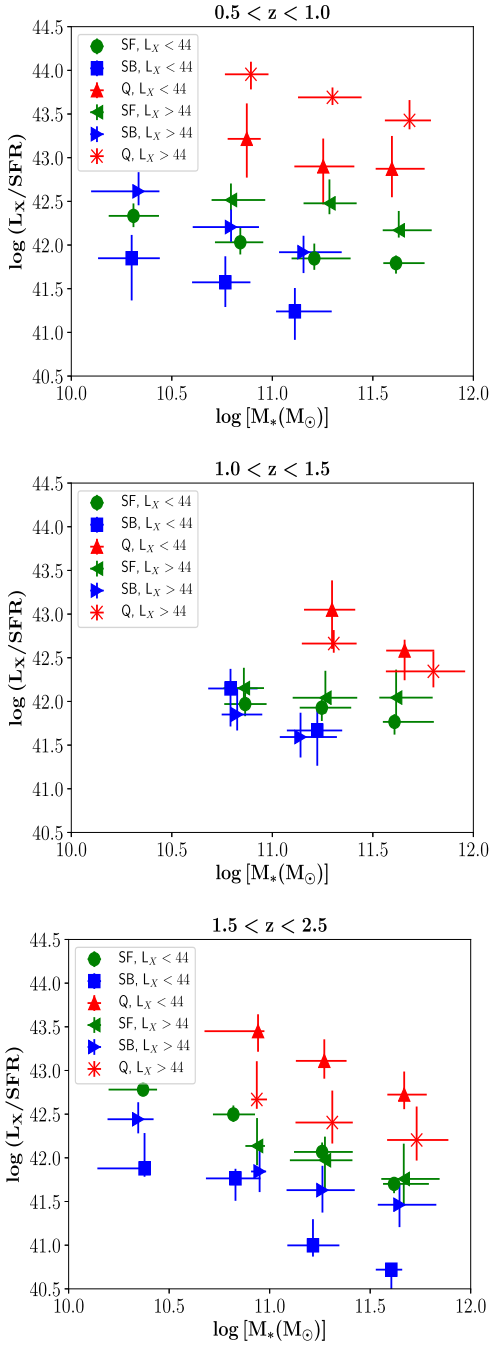

Figure B2. The difference of the amplitude of L_X/SFR between luminous AGN ($\log[L_{X,2-10\,keV}(ergs^{-1})] > 44$) and low-to-moderate luminosity AGN ($\log[L_{X,2-10\,keV}(ergs^{-1})] < 44$). At $0.5 < z < 1.0$ luminous AGN have higher L_X/SFR values compared to their lower L_X counterparts, for all AGN host galaxy classifications. At higher redshifts, luminous AGN hosted by Q systems present a lower L_X/SFR compared to lower L_X sources.

In Fig. B2, we examine the ratio log(L_X/SFR) as a function of M_*, for luminous and low to moderate L_X AGN. We find similar trends for both AGN populations, with luminous sources to have higher log(L_X/SFR) amplitude compared to less luminous X-ray sources, at low redshifts. However, at higher redshifts, luminous AGN hosted by Q galaxies present a lower log(L_X/SFR) amplitude compared to their lower L_X counterparts. To investigate this behaviour further, in Fig. B3, we plot the L_X versus SFR for the two AGN populations.

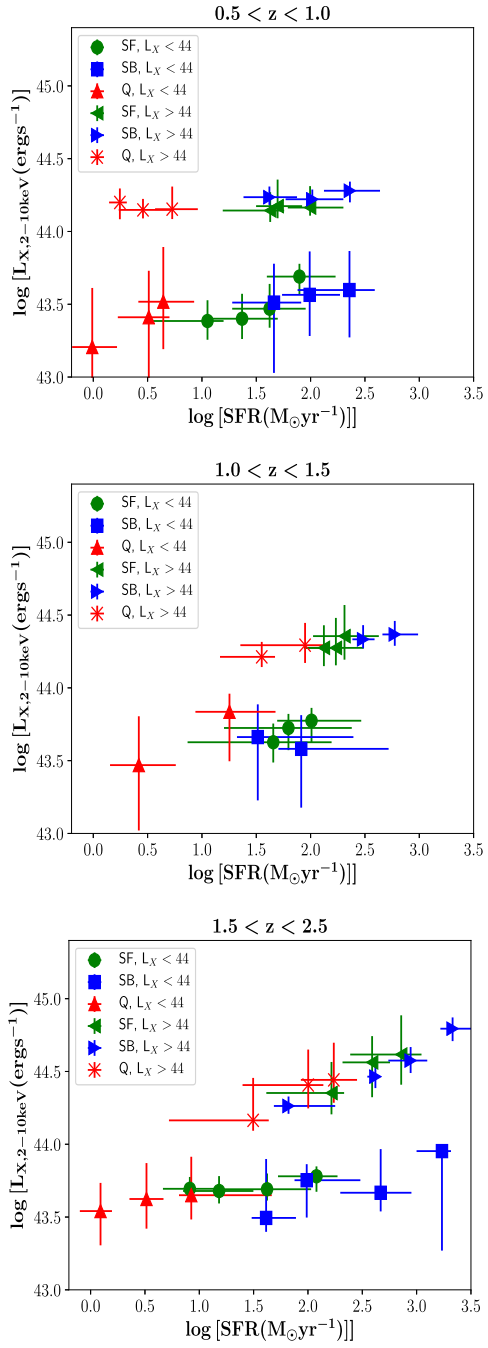

Figure B3. L_X as a function of SFR for SB, SF, and Q AGN host galaxies, at three redshift intervals, for luminous and low-to-moderate L_X AGN. At low redshifts (top panel), both AGN populations have similar SFR. However, at high redshifts (bottom panel) this is true only for the SB systems.

Based on these results, at low redshifts (top panel of Fig. B3), for all AGN host galaxy classifications, luminous and less luminous AGN have similar SFR. At higher redshifts (bottom panel of Fig. B3) this is true only for the SB galaxies, whereas Q systems that host less luminous AGN have significant lower SFR (by ∼1 dex) compared to their more luminous counterparts.

This paper has been typeset from a TEX/LATEX file prepared by the author.